

Fabrication of Strontium Titanate Thin Film with Pre-crystallized Layer via Sol-Gel Spin Coating Method

Kelvin Voon Yan Jie^{1,*}, Mohd Fairus Ahmad^{1,2}, Muhammad Mahyiddin Ramli^{1,2}, Safizan Shaari¹, Arif Mawardi Ismail¹, and Yusran Sulaiman^{3,4}

¹Faculty of Electronic Engineering Technology, Universiti Malaysia Perlis, Perlis, Malaysia

²Institute of Nano Electronic Engineering, Universiti Malaysia Perlis, Perlis, Malaysia

³Department of Chemistry, Faculty of Science, Universiti Putra Malaysia, UPM Serdang, Selangor, Malaysia

⁴Functional Devices Laboratory, Institute of Nanoscience and Nanotechnology, Universiti Putra Malaysia, UPM Serdang, Selangor, Malaysia

ABSTRACT

The technique of pre-crystallized layer is introduced in the strontium titanate (STO) thin film fabrication to improve the coating thickness and the crystallinity. The STO thin films were fabricated on glass substrates via the spin coating method with STO precursor solution that was synthesized through the sol-gel process. The characteristics of the thin films were analyzed through X-ray diffraction (XRD) analysis, profilometry, UV-Vis spectra analysis and scanning electron microscopy (SEM) analysis. In the present study, the samples of 20 layers and 25 layers (deposited on the pre-crystallized layer) exhibited better crystallinity as compared with the samples of 5 layers, 10 layers and 15 layers (without the pre-crystallized layer). The samples of 25 layers exhibited the highest film thickness (224 nm), highest absorbance intensity and the highest XRD peak intensity at 32, 40, 47 and 58°, which represent the planes (110), (111), (200) and (210), respectively. The pre-crystallized layer served as the mechanical support for further layer deposition.

Keywords: Pre-crystallized layer, sol-gel method, spin coating method, strontium titanate

1. INTRODUCTION

Photovoltaic (PV) technology has attracted much interest as a potential approach for generating sustainable energy due to the raised global awareness of the requirement for carbon-neutral energy production for environmental sustainability [1]. As compared with other renewable energy sources [2] and fossil-based conventional energy sources, solar energy is rather abundant, delivering several kilowatt-hours per square meter daily [3]. There are different types of PV technologies: crystalline silicon (Si) cells, perovskite cells, dye-sensitized solar cells (DSSC) [4,5,6,7,8], thin film cells, organic cells, and inorganic cells.

Among many of the PV technologies, the perovskite-based PV technology has received a lot of attention due to its large bandgap for utilizing higher energy photons for energy conversion and generating higher open-circuit voltage (VOC). Similar to the conventional Si-based PV cell, a perovskite-based PV cell can be engineered to utilize a wider spectrum (visible, infrared and UV), which allows a higher conversion of the sunlight absorbed into electricity. A perovskite is a material with a crystal structure of ABX_3 , which is the same as the first-discovered mineral perovskite, calcium titanium oxide ($CaTiO_3$). Recently, the use of perovskite strontium titanate (STO) was reported to be approaching 100% quantum efficiency of the photon to electron conversion in a photocatalytic reaction [9]. STO has the advantages of high chemical and thermal stability. Thus, it appears as a promising candidate for efficient fuel cells, solar cells, and

* kelvinvoon@studentmail.unimap.edu.my

photocatalyst applications. Furthermore, the devices can also be fabricated in an ambient atmosphere.

There are different types of thin film fabrication methods such as spin coating method [10,11], dip coating method [12,13], physical vapor deposition [14] and chemical vapor deposition [15,16]. Perovskite material thin film can be fabricated through its precursor in the form of sol-gel which typically utilized the spin coating method and dip coating method. Thin film fabrication through spin coating method has advantages to fabricate significantly fine, thin, and uniform coating, even provide simplicity for large area sample [17].

In this study, we will demonstrate the method of STO synthesis through the sol-gel method and STO thin film fabrication with a pre-crystallized layer deposited through the spin coating method. Then, we analyze the films properties based on the layer thickness and the effect of heat treatment. The samples will be analyzed through X-ray diffraction (XRD) analysis, surface profilometry, UV-Vis spectra analysis and scanning electron microscopy (SEM) analysis.

2. MATERIAL AND METHODS

2.1 Synthesis of Strontium Titanate

Synthesis of STO powder: The STO powder was synthesized based on a previous study in [10]. Similar to the study, 3 mmol of strontium nitrate ($\geq 99.0\%$) was added in 5 ml of distilled water, forming clear colourless solution. Equimolar of titanium diisopropoxide bis(acetylacetonate) (75 wt. % in isopropanol) was then added to obtain a cloudy and slightly orange solution. 2 mmol of citric acid ($\geq 99.5\%$) dissolved in 10 ml of distilled water was then added to promote homogeneity and hydrolysis reaction [18]. 2 mmol Ethylene glycol (99.8 %) was added to promote polymerisation between titanium ion and strontium nitrate. With further heating under 100 °C, the STO crystallized powder coloured in white could be obtained. All the chemical reagents were purchased from the Sigma-Aldrich company. The chemicals were used without any additional purification.

Synthesis of STO precursor sol-gel: The synthesized powder was insoluble in the DMSO solvent. The previous technique in [4] was modified to synthesize the STO precursor sol-gel solution. The molar ratio of titanium ion, citric acid and ethylene glycol was modified to be 1:4:16 [12]. In this study, the molar ratio between citric acid and strontium ion was [4:1], where a higher molar ratio of citric acid and strontium ion is needed to enhance the homogeneity of the sol gel network [18]. The mixed precursor solution was heated at 70 °C under constant stirring for 3 days to form the pale yellowish sol-gel STO precursor solution.

2.2 Synthesis of Strontium Titanate

The glass substrate was cleaned using an ultrasonic bath with the following solvents: acetone, isopropyl alcohol, ethanol and DMSO. The cleaning interval was set at 15 minutes for each solvent. The size of the glass substrate is 20 mm \times 20 mm, with the thickness of 0.13 – 0.17 mm.

The synthesized STO precursor gel was dissolved in DMSO solvent with a concentration of 3 g/ml. 100 μ L of the solution was dropped on the substrate by using a micropipette. The spin coating step was started at 200 rpm for 30 s to spread the solution over the substrate. The spin coating step was continued with 2000 rpm for 30 s, followed by 5000 rpm for 30 s. The multilayer thin film was spin coated on the substrate subsequently with the introduction of a drying process for each coated film layer. Before dropping another solution to form a subsequent layer, the solvent of each layer must be evaporated to prevent the trapping of the solvent in the coated layer. Since the solvent used in our case is DMSO, which is not volatile in the ambient atmosphere (DMSO has

a boiling point of 189°C), the DMSO evaporation process was carried out by drying the thin film on the hot plate (180°C for 15 mins each layer). (Note: Drying over the boiling point of the solvent will cause solvent to boil, resulting the bubble formation destroying the uniformity of the thin film.) After all the multilayer thin film coating had been completed, the samples went through the heat treatment process (2 hours under 300°C in the tube furnace) and the crystallization process (2 hours under 500°C in the tube furnace). Five STO thin film samples were prepared as follows: 5 layers, 10 layers, 15 layers, 20 layers and 25 layers. The samples of 5 layers, 10 layers and 15 layers undergo the process of heat treatment and crystallization after all the layers were deposited, whereas the samples of 20 layers and 25 layers were started from the first 5 layers of the thin film, which had undergone the crystallization process to form a pre-crystallized STO layer. Since a thicker STO thin film was desired, pre-crystallization was not performed for samples with 10 and 15 layers.

2.3 Characterization

The phase evaluation and structural information of the as-synthesized powder and thin films were characterized by X-ray diffraction (XRD). The XRD analysis was carried out using Bruker D2 phaser with Cu-K α radiation (1.54184 Å), which was set up at current and voltage settings of 10 mA and 30 kV, respectively. The XRD data were obtained within the interval range of $10^\circ \leq 2\theta \leq 80^\circ$ at a scanning speed of 11.2°/min.

The thickness of the spin coated STO thin films was characterized by profilometry machine (Bruker DektakXT) A portion of the coated surface was removed through mechanical force with a blade, where the substrate region was exposed. The film thickness was measured through a difference between the coated surface and the removed surface.

The optical properties of the thin films were characterized by UV-Vis spectroscopy machine (Perkin Elmer Lambda 950 UV-Vis-NIR). The absorbance analysis was performed from the wavelength range of 250 nm until 650 nm at a scanning speed of 266.75 nm/min.

The surface morphological properties of the thin films were characterized by scanning electron microscopy (SEM). The morphological study of the thin films was performed on Hitachi TM 400 Plus II Tabletop Microscope with an operating acceleration voltage of 15 kV. The surface morphology of the samples was observed at the magnification of $\times 100$, $\times 1000$ and $\times 3000$.

3. RESULTS AND DISCUSSION

3.1 XRD Analysis

The XRD result of the as-synthesized STO powder is shown in Figure 1. The XRD reference data was extracted from Material Project data [19]. STO characteristic peaks are detected at 23, 32, 40, 47, 58, 69, 71 and 77°, which represent the planes (100), (110), (111), (200), (210), (211), (300) and (310), respectively (Material ID: mp-5229). The rest of the peaks are assumed to be the unreacted strontium nitrate (Material ID: mp-4157). According to [10], the characteristic of the excess amounts of strontium nitrate could be minimized through several rinses with a DMSO/DMF solvent. According to the study in [18], there would be an excess amount of unreacted strontium nitrate when the molar ratio of citric acid to strontium ion is smaller than 1. In our case, the molar ratio is [2:3].

The XRD result of the five samples of spin coated STO thin film is shown in Figure 2. The thin film sample of 25 layers exhibits STO characteristic peak at 32, 40, 47 and 58°, which represent the planes (110), (111), (200) and (210), respectively, while showing background data for the glass substrate. Additionally, there is no peak for the strontium nitrate as found in the powder (Figure

1), indicating it was washed out by DMSO during the spin coating. The sample of 25 layers shows the highest peak intensity among all the five samples, followed by the samples of 20 layers and 5 layers. The samples of 20 layers and 25 layers consisted of the pre-crystallized layer, which acted as a mechanical support for further layer deposition. On the other hand, there are little or none of the STO characteristics shown for the samples of 10 layers and 15 layers, which might be due to their lack of crystalline phase, or the film coated is too thin to be detected. The case here is compatible with the study conducted in [12], where the samples with higher coating layers exhibited weaker STO characteristics compared with the samples with lower coating layers. The effect was explained as the sample requires a higher annealing temperature for each increasing number of layers to support the reaction in a high concentration of STO precursor. However, the explanation is not apparent in our case for the samples of 25 layers and 20 layers, since the drying, heat treatment and crystallization process conditions are maintained. Therefore, such a pre-crystallized layer had improved the crystallinity of the higher number of coating layers.

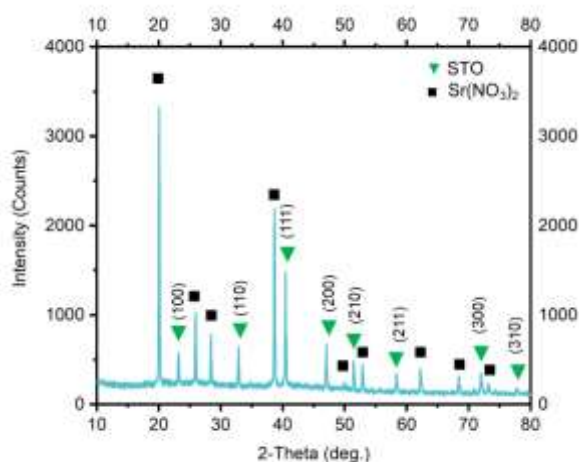


Figure 1. XRD graph of as-synthesized STO powder, showing the respective peaks of STO and $\text{Sr}(\text{NO}_3)_2$.

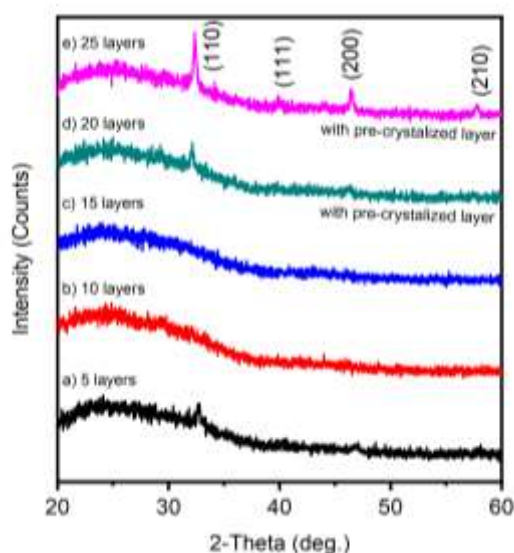


Figure 2. XRD graph of STO thin film samples: (a) 5 layers (b) 10 layers (c) 15 layers (d) 20 layers (e) 25 layers. The samples of (a), (b) and (c) undergo crystallization process after all the layers were coated; while the samples of (d) and (e) had undergone one one-time crystallization process for the first 5 layers coated.

3.2 Surface Profilometry

Surface profilometry was used to measure the thickness of the thin film samples. The relationship between the measured thickness and the number of layers coated is shown in Figure 3 and summarized in Table 1. The data confirms that the samples of 10 layers and 15 layers have a coated STO layers, which could not be confirmed by the XRD data. Moreover, the thickness of samples of 10 layers and 15 layers is lower as compared with the sample with 5 layers, indicating the further deposited layers showed a decreased thickness. This also supports that there was a weak adhesion of the STO precursor solution on the STO layer without a pre-crystallization layer. However, the samples of 20 layers and 25 layers show a linear relationship between the thickness measured and the number of layers spin coated. It is suspected that the pre-crystallized layers provided better adhesion for the subsequent spin coated layers, probably due to higher surface energy as compared to the glass substrate surface.

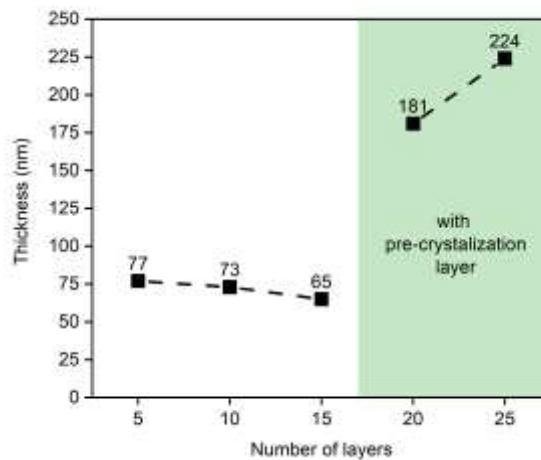


Figure 3. Plotted graph of the thickness of the coated thin film measured through the profilometer versus the number of layers spin coated.

3.3 Scanning Electron Microscopy

As shown in Figure 4, the morphological of the five samples were investigated under scanning electron microscopy. The sample of 5 layer shows aggregation on the uppermost layer, which is due to the high heating rate in the tube furnace causing the amorphous phase of the layers to coagulate and results in the shrinkage spot. This defect could be minimized by reducing the heating rate for the heat treatment and crystallization process. The samples of 10 layers, 15 layers and 20 layers indicate the presence of the amorphous phase. It could explain the weak STO characteristic shown in the XRD analysis. The sample of 25 layers show significant microcrack and flaking surface defects. The microcrack defect is dependent on the coating thickness, where the microcrack defect occurs more significantly as the coating thickness was increased [20]. It can be observed from the comparison of the samples with 20 layers and 25 layers under the same magnification of $\times 3000$. The microcrack defect could be minimized by implementing the multilayer coating of the low concentration solution rather than a single layer coating of the high concentration solution, given that the same thickness was achieved [21]. The flaking defect occurs in the sample of 25 layers indicates that the poor adhesion with the underneath layer causes the detachment of the uppermost layer. Impurities on the underneath layer could contribute to the factor of the flaking defect.

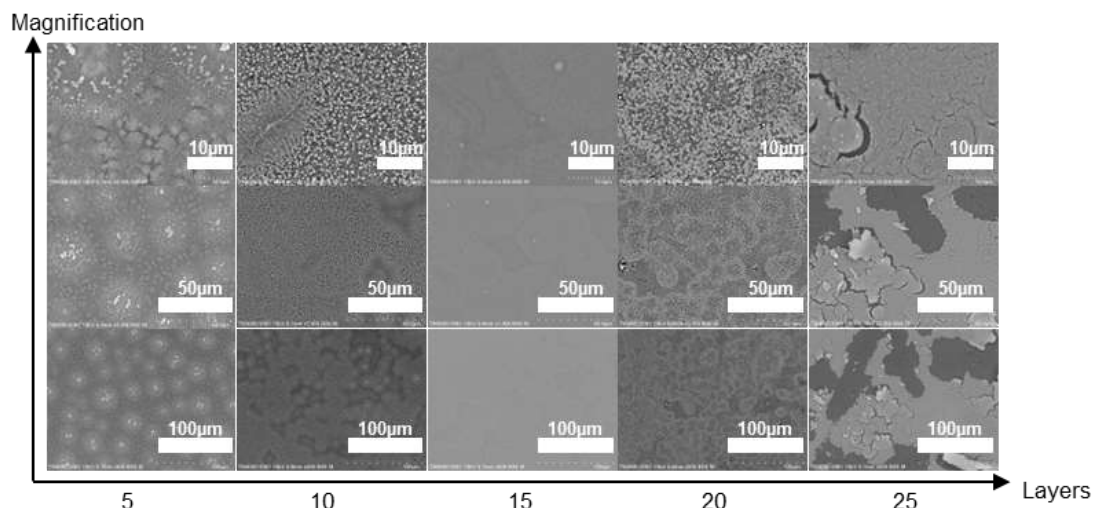


Figure 4. SEM images of the STO thin film samples with the number of coated layers increased along the horizontal axis (5 layers, 10 layers, 15 layers, 20 layers and 25 layers); and the magnification increased along the vertical axis ($\times 100$, $\times 1000$ and $\times 3000$).

3.4 UV-Vis Spectra Analysis

The optical absorbance graph for the five samples is shown in Figure 5(a). The sample of 15 layers has the lowest absorbance among the samples. The absorbance data is in agreement with the measured thickness of the samples from the surface profilometer showed in Table 1, where the absorbance intensity increased as the coated thickness increased.

The optical absorption coefficient (α) is obtained from the absorbance spectral data extracted by applying the Beer-Lambert law equation **Error! Reference source not found.**

$$I = I_0 e^{-\alpha x} \tag{1}$$

Hence

$$\alpha = \frac{2.303}{x} \log \left(\frac{I}{I_0} \right) = 2.303 \left(\frac{A}{x} \right) \tag{2}$$

where I is the intensity of the transmitted light, I_0 is the intensity of the incident light, A is the absorbance and x is the sample thickness, where in this case is the film thickness measured using profilometer as shown in Table 1.

Table 1 Data of the thin film samples showing the measured thickness, absorption edges, direct bandgap and indirect bandgap

Number of Layers	Measured Thickness (nm)	Absorption Edges (eV)	Direct Bandgap (eV)	Indirect Bandgap (eV)
5	77	3.90 (=318 nm)	4.06	3.78
10	73	3.91 (=317 nm)	4.07	3.82
15	65	3.95 (=313 nm)	4.10	3.87
20	181	3.88 (=320 nm)	4.05	3.73
25	224	3.86 (=321 nm)	4.03	3.67

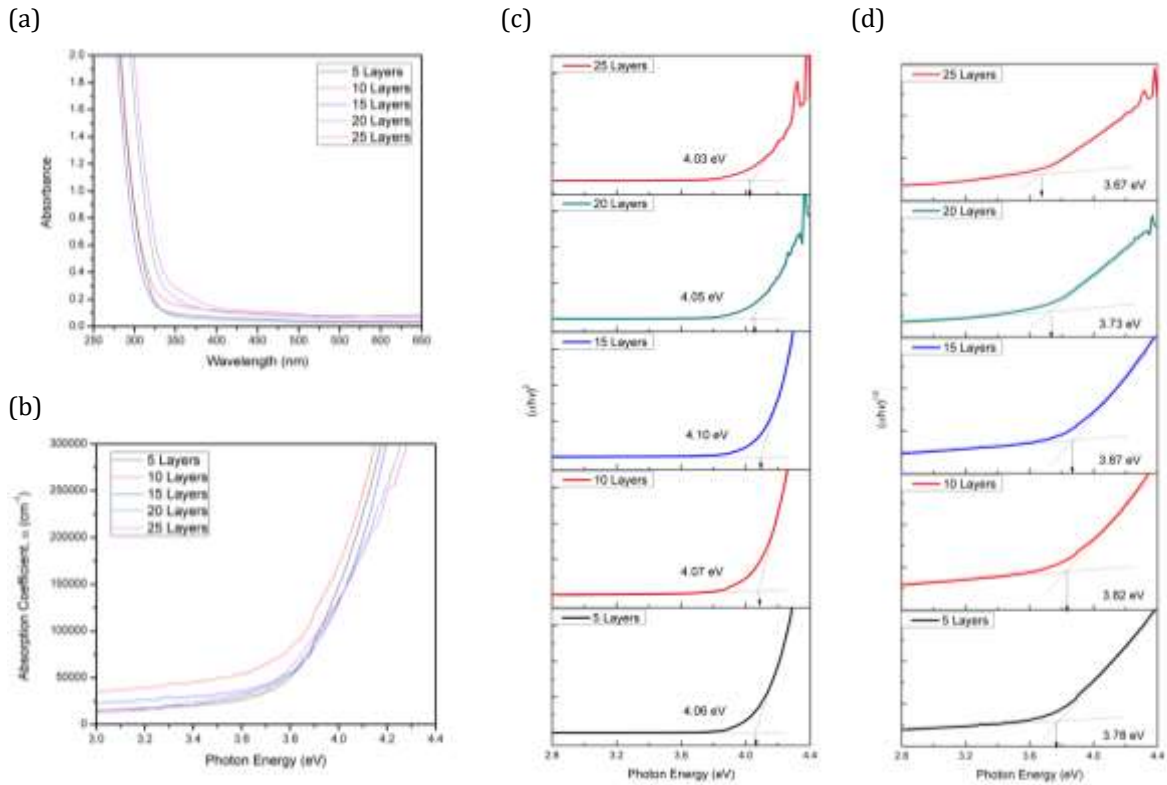


Figure 5. (a) Absorbance graph versus wavelength (b) Absorption coefficient versus photon energy of the STO thin film samples of 5 layers, 10 layers, 15 layers, 20 layers and 25 layers. Linear extrapolation of the graph of (c) Direct energy bandgap (d) Indirect energy bandgap.

The absorption edge values for the samples were obtained through the linear extrapolation of the optical absorption coefficient against the photon energy to the zero-absorption value, which was plotted in Figure 5(b). The absorption edge values of the samples are shown in Table 1, showing that the absorption edge value decreased as the thickness increased. The absorption edge values range from 3.86 eV to 3.95 eV.

The Tauc method is used to estimate the bandgap energy of the samples using the optical absorption spectra data [22,23]. This method assumes that the energy-dependent absorption coefficient α can be defined with the equation **Error! Reference source not found.:**

$$(\alpha h\nu)^{1/\gamma} = B(h\nu - E_g) \quad (3)$$

where h is the Planck constant, ν is the frequency of the photon, E_g is the bandgap energy and B is the constant. The γ factor depends on the nature of the electron transition, where it represents direct and indirect transition bandgaps with a factor value of $\frac{1}{2}$ or 2, respectively [23]. Direct and indirect energy bandgap are obtained through the linear extrapolation of the graph of $(\alpha h\nu)^2$ against $h\nu$ and the graph of $(\alpha h\nu)^{1/2}$ against $h\nu$, respectively.

The graphs of the direct energy bandgap and indirect energy bandgap are shown in Figure 5(c) and (d). Both types of energy bandgap values exhibit the same dependence on the thin film thickness. The direct bandgap values range from 4.03 eV to 4.10 eV, while the indirect bandgap values range from 3.67 eV to 3.87 eV. The bandgap energy values obtained from absorption edges, direct bandgap and indirect bandgap methods are higher than the bandgap of STO crystal (3.37 eV – 3.41 eV) as mentioned in [24]. It was also mentioned that there are two possible explanations for the difference in energy bandgap values: (1) The existence of an additional electric field due to the presence of the grain boundaries in the polycrystalline thin film, which then increased the

bandgap energy; and (2) the formation of electronic charged defects due to the presence of oxygen vacancies. Therefore, in this present study, the poor crystallinity of the samples may be accountable for the difference in bandgap energy as it showed the presence of amorphous phases and surface defects in a higher thickness sample (Figure 4).

4. CONCLUSION

In summary, this study demonstrated the fabrication method by using the spin coating method with STO precursor solution that was synthesized through the sol-gel process. We also demonstrated the analysis of the thin films through XRD analysis, profilometry, UV-Vis spectra analysis and SEM analysis. The samples of 25 layers exhibited the highest film thickness (224 nm), highest absorbance intensity and the highest XRD peak intensity at 32, 40, 47 and 58°, which represent the planes (110), (111), (200) and (210), respectively. The morphological study showed microcrack and flaking defects on the sample of 25 layers, which is a challenge for a high thickness sample. The amorphous state present in the other samples also indicates insufficient heating. In this study, the pre-crystallized layer was introduced to improve the coating thickness, as shown in the samples of 20 layers and 25 layers, which show a better film property.

ACKNOWLEDGEMENTS

The authors acknowledge the Center of Excellence for Frontier Materials Research, Universiti Malaysia Perlis and the financial support by the Ministry of Higher Education Malaysia through the Fundamental Research Grant Scheme 2021 (FRGS Grant No.: FRGS/1/2021/TK0/UNIMAP/02/58).

REFERENCES

- [1] N.S. Lewis, Toward cost-effective solar energy use, *Science* (1979), vol. 315, no. 5813, pp. 798–801, 2007, doi: 10.1126/science.1137014.
- [2] Z. Zailan, S.R. Kasjoo, N.F. Zakaria, M.M. Isa, M.K.M. Arshad, and S. Taking, Rectification performance of self-switching diodes in silicon substrate using device simulator, 2016 3rd International Conference on Electronic Design, ICED 2016, pp. 373–376, 2017, doi: 10.1109/ICED.2016.7804671.
- [3] T.F. Schulze et al., Efficiency enhancement of organic and thin-film silicon solar cells with photochemical upconversion, *Journal of Physical Chemistry C*, vol. 116, no. 43, pp. 22794–22801, Nov. 2012, doi: 10.1021/jp309636m.
- [4] M. Mazalan, M.M. Noh, Y. Wahab, M.N. Norizan, and I.S. Mohamad, Development of dye-sensitized solar cell (DSSC) using patterned indium tin oxide (ITO) glass: Fabrication and testing of DSSC, CEAT 2013 - 2013 IEEE Conference on Clean Energy and Technology, pp. 187–191, 2013, doi: 10.1109/CEAT.2013.6775624.
- [5] N.A. Norhisamudin et al., The Effect of Different Solvents in Natural Dyes from Roselle (*Hibiscus Sabdariffa*) and Green Tea Leaves (*Camellia Sinensis*) for Dye-Sensitized Solar Cell, *J Phys Conf Ser*, vol. 1755, no. 1, 2021, doi: 10.1088/1742-6596/1755/1/012024.
- [6] N. Jamalullail, I.S. Mohamad, M.N. Norizan, N. Mahmed, and B.N. Taib, Recent improvements on TiO₂ and ZnO nanostructure photoanode for dye sensitized solar cells: A brief review, *EPJ Web Conf*, vol. 162, pp. 1–5, 2017, doi: 10.1051/epjconf/201716201045.
- [7] I.S. Mohamad, M.N. Norizan, M.K.F.M. Hanifah, I.A.M. Amin, and M.M. Shahimin, Fabrication and characterization of ZnO:In thin film as photoanode for DSSC using natural fruit dyes, *AIP Conf Proc*, vol. 1660, 2015, doi: 10.1063/1.4915767.

- [8] N.A. Norhisamudin et al., The efficiency effect of dye sensitized solar cell using different ratio of organic polymer doped titanium dioxide at different annealing process temperature, *AIP Conf Proc*, vol. 2203, 2020, doi: 10.1063/1.5142144.
- [9] T. Takata et al., Photocatalytic water splitting with a quantum efficiency of almost unity, *Nature*, vol. 581, no. 7809, pp. 411–414, 2020, doi: 10.1038/s41586-020-2278-9.
- [10] M. Neophytou et al., Enhancing the Charge Extraction and Stability of Perovskite Solar Cells Using Strontium Titanate (SrTiO₃) Electron Transport Layer, *ACS Appl Energy Mater*, 2019, doi: 10.1021/acsaem.9b01567.
- [11] X. Zhu et al., Chemical solution deposition of LaMnO₃ buffer layers for coated conductors, *IEEE Transactions on Applied Superconductivity*, vol. 17, no. 4, pp. 3880–3885, 2007, doi: 10.1109/TASC.2007.910165.
- [12] S. Maarof, K. Deraman, W.N.W. Shamsuri, B. Ismail, and S.A. Mat, *Malaysian Journal of Fundamental and Applied Sciences Microstructure Studies of Strontium Titanate Thin Films Prepared by Sol-gel Dip Coating Method*, pp. 134–138, 2013.
- [13] C. Xu, J. Huang, X. Tan, T. Yu, Z. Cui, and L. Zhao, Preparation, characteristics, and photocatalytic tests of Fe-doped TiO₂ films prepared by a sol-gel dip coating via homemade devices, *J Dispers Sci Technol*, vol. 31, no. 12, pp. 1732–1739, 2010, doi: 10.1080/01932690903543097.
- [14] F.U. Hamelmann, Thin film zinc oxide deposited by CVD and PVD, *J Phys Conf Ser*, vol. 764, no. 1, 2016, doi: 10.1088/1742-6596/764/1/012001.
- [15] S.A. Abdul Rais et al., Effect of indium pre-flow on wavelength shift and crystal structure of deep green light emitting diodes, *Opt Mater Express*, vol. 11, no. 3, p. 926, 2021, doi: 10.1364/ome.413417.
- [16] S.A. bin Abdul Rais et al., Fabrication of Deep Green Light Emitting Diode on Bulk Gallium Nitride Substrate, *J Phys Conf Ser*, vol. 1535, no. 1, 2020, doi: 10.1088/1742-6596/1535/1/012016.
- [17] A. Mishra, N. Bhatt, and A.K. Bajpai, Nanostructured superhydrophobic coatings for solar panel applications. Elsevier Inc., 2019. doi: 10.1016/B978-0-12-815884-5.00012-0.
- [18] J.H. Lopes, O.M.V.M. Bueno, I.O. Mazali, and C.A. Bertran, Investigation of citric acid-assisted sol-gel synthesis coupled to the self-propagating combustion method for preparing bioactive glass with high structural homogeneity, *Materials Science and Engineering C*, vol. 97, pp. 669–678, 2019, doi: 10.1016/j.msec.2018.12.022.
- [19] A. Jain et al., Commentary: The materials project: A materials genome approach to accelerating materials innovation, *APL Mater*, vol. 1, no. 1, 2013, doi: 10.1063/1.4812323.
- [20] G.C. da Costa et al., Effect of viscosity and temperature on the microstructure of BBT thin films, *Materials Research*, vol. 6, no. 3, pp. 347–351, 2003, doi: 10.1590/s1516-14392003000300008.
- [21] J.H. Prosser, T. Brugarolas, S. Lee, A.J. Nolte, and D. Lee, Avoiding cracks in nanoparticle films, *Nano Lett*, vol. 12, no. 10, pp. 5287–5291, 2012, doi: 10.1021/nl302555k.
- [22] N.F. Mott and E.A. Davis, Conduction in non-crystalline systems V. Conductivity, optical absorption and photoconductivity in amorphous semiconductors, *Philosophical Magazine*, vol. 22, no. 179, pp. 903–922, 1970, [Online]. Available: <https://doi.org/10.1080/14786437008221061>
- [23] P. Makuła, M. Pacia, and W. Macyk, How To Correctly Determine the Band Gap Energy of Modified Semiconductor Photocatalysts Based on UV-Vis Spectra, *Journal of Physical Chemistry Letters*, vol. 9, no. 23, pp. 6814–6817, 2018, doi: 10.1021/acs.jpcllett.8b02892.
- [24] Y. Gao, Y. Masuda, and K. Koumoto, Band Gap Energy of SrTiO₃ Thin Film Prepared by the Liquid Phase Deposition Method, *Journal of the Korean Ceramic Society*, vol. 40, no. 3, pp. 213–218, 2003, doi: 10.4191/kcers.2003.40.3.213.

